RSC Advances

PAPER

View Article Online
View Journal | View Issue

Cite this: *RSC Adv.*, 2026, **16**, 8388

Temperature-mediated microstructure evolution and densification mechanism of F2314 fluoropolymer binder during warm isostatic pressing

Baogang Yang,[ab] Kai Yang,[b] Zhijian Yang,[b] Kezhn Lv,[b] Haiying Yang,[c] Jiang Li*[a] and Shaoyun Guo[a]

Polymer-bonded explosives (PBX) incorporate a fluoropolymer binder (F2314) as a critical component. The densification behavior of F2314 influences the microstructure and macroscopic properties of PBX, thereby determining the service performance of PBX components. A series of samples was prepared by isostatic pressing at temperatures between 65 and 140 °C to elucidate the influence of the compaction temperature on the densification mechanism of F2314. The results indicated that F2314 underwent successive phase transitions during heating, which included glass transition, cold crystallization, and partial melting. The crystallinity of F2314 initially increased, then decreased, accompanied by a progressive decline in the content of rigid segments. Increasing the compaction temperature significantly enhanced densification of the F2314 specimens, increasing the relative density from 88.6% to 99.5%, with stabilization above 95 °C. A distinct transition from brittle to ductile fracture behavior was observed between 95 and 110 °C, whereas the glass transition temperature and apparent activation energy remained relatively stable. The densification mechanism transitioned from mechanical interlocking at the particle scale at lower temperatures to the formation of an interpenetrating network structure at elevated temperatures. This transition was driven by enhanced molecular chain mobility, flow, and interdiffusion. In terms of process safety and mechanical performance, 125 °C was identified as the optimal compaction temperature for F2314. These findings establish a fundamental correlation among temperature, microstructure, and properties to provide a scientific basis for the optimized isostatic pressing of F2314-based PBX.

Received 21st December 2025
Accepted 29th January 2026

DOI: 10.1039/d5ra09872f

rsc.li/rsc-advances

Introduction

Polymer-bonded explosives (PBX) are a class of high-energy composite materials that integrate crystalline explosive particles with a polymeric binder and various additives. PBX serves as a critical energy source and a structural component in modern weapon systems, with its performance and reliability being paramount.[1–4] The microscale behavior of the polymeric binder plays a crucial role in determining the macroscopic reliability of PBX, as it governs the integration of discrete explosive crystals into a mechanically coherent and stable structure. The thermoplastic random fluoropolymer (F2314), synthesized from vinylidene fluoride (VDF) and chlorotrifluoroethylene (CTFE) at a 1 : 4 molar ratio, is widely used as a polymeric binder due to its favorable combination of thermal stability, chemical resistance, and mechanical flexibility.[5–11] Consequently, the binder is decisive in determining the mechanical integrity, safety, and ultimate performance of PBX components under operational conditions.[12,13]

Warm-isostatic pressing (WIP) is a pivotal manufacturing technique for PBX and offers significant advantages, including the production of components with minimal internal defects and enhanced safety. In accordance with Pascal's law, WIP employs a fluid medium to apply uniform pressure from all directions to the explosive particles contained within a flexible mold. Additionally, this enables efficient near-net-shape formation of complex geometries while effectively mitigating density gradient issues commonly encountered in conventional uniaxial pressing.[14–18] In conventional molding processes, uniaxial stresses typically induce the orientation of microstructures within the bonded phase. In contrast, WIP facilitates the uniform rearrangement of polymer molecular chains *via* isotropic heat-force coupling, thereby promoting the development of isotropic microstructures. Consequently, WIP has

[a]State Key Laboratory of Advanced Polymer Materials, Polymer Research Institute of Sichuan University, Chengdu, 610065, China. E-mail: li_jiang@scu.edu.cn
[b]Institute of Chemical Materials, China Academy of Engineering Physics, Mianyang, 621900, China
[c]Mianyang Ecological Environment Bureau, Mianyang, 621000, China

become an indispensable high-end manufacturing technology for PBX processing. During WIP, beyond the physical rearrangement and fragmentation of explosive crystals, the F2314 binder undergoes intense microstructural evolution as the continuous phase. Moreover, the macroscopic mechanical properties, dimensional stability, and long-term storage reliability of the final PBX component are fundamentally governed by conformational adjustments, entanglement/disentanglement, and phase transitions of the molecular chains, which are part of the microstructural evolution.

However, research on PBX has historically focused on the synthesis, control of crystal morphology, surface modification, and compaction behavior of explosive crystals. In contrast, studies on polymer binders, particularly high-performance F2314, are relatively rare in terms of number and depth. Critical aspects such as the evolution of the binder's condensed-state structure and its intrinsic response under coupled thermal-mechanical conditions during WIP remain poorly understood. Although prior work has examined binder-crystal interfacial interactions, material modification, aging, and crystallization behavior,[19–26] these efforts have not provided comprehensive insights into the microstructural evolution and densification mechanisms of F2314 under processing-relevant conditions. The absence of a comprehensive mechanistic understanding hinders the rational design of binder-dominated consolidation processes and constitutes a significant barrier to the reliable, high-performance manufacturing of PBX components.

As a typical thermoplastic, F2314 exhibits highly temperature-sensitive molecular chain dynamics. The temperature sensitivity results in markedly different macroscopic properties in the PBX components formed at different WIP temperatures. Although previous rheological models have attempted to describe the flow behavior of polymer binders under processing conditions, they often fail to entirely capture the nonlinear viscoelastic response and structural evolution of F2314 under actual WIP conditions. The lack of a precise understanding of the binder's rheological behavior under WIP conditions hinders the establishment of quantitative correlations between processing temperature and the microstructure/properties of PBX. Therefore, macroscopic cracks, localized pores, and insufficient mechanical strength are common in formed explosive components, compromising their mechanical integrity and service reliability.

Therefore, this study aimed to address this challenge and systematically investigated the "temperature-structure-property" relationships in the F2314 binder during isostatic pressing. The F2314 specimens were prepared using WIP over a 65–140 °C temperature range. The F2314 specimens were prepared using WIP within the temperature range of 65–140 °C, covering the binder's critical transition from the highly elastic state to the viscous-flow state during actual processing. An array of techniques was used to characterize the dynamic evolution of the condensed-state structure, molecular chain mobility, mechanical properties, and viscoelasticity. The findings of this study are expected to clarify the PBX densification mechanism during WIP and provide crucial theoretical guidance for the high-quality manufacturing of isostatically pressed PBX components.

Experimental

Materials

The F2314 random copolymer (VDF : CTFE molar ratio = 1 : 4) was procured from a commercial supplier. The as-received white solid powder exhibited M_n and M_v values of 2.9×10^5 and 5.2×10^5 g mol^{-1}, respectively. The particle size distribution ranged from 7 to 75 μm with a D_{50} of 34.0 ± 15.6 μm (as shown in Fig. S1). The powder was used as received without further purification. Throughout the sample preparation and WIP processes, all operations were carried out in a controlled dry atmosphere with precise temperature regulation to minimize moisture absorption and thermal-oxidative degradation.

Compaction equipment

An isostatic press (Institute of Chemical Materials, CAEP) with a maximum operating pressure of 300 MPa and a maximum operating temperature of 300 °C was used for isostatic pressing. The rates of pressure application and release were adjustable within the range of 1–20 MPa min^{-1}.

Specimen preparation

The F2314 specimens were fabricated using isostatic pressing (Fig. 1). The detailed procedure is as follows: first, the raw F2314 powder was placed into a flexible mold and vibrated to achieve a densely packed initial state. The mold was subsequently transferred to an oven and heated to the target temperature (65, 80, 95, 110, 125, or 140 °C). The mold was vacuum-sealed upon reaching the target temperature. The sealed assembly was placed into an isostatic press, with the pressure-transmitting medium maintained at the same temperature as the sample. A pressure of 100 MPa was applied, and the mixture was held for 60 min. The pressure rise and release rates were 8 MPa min^{-1} and 4 MPa min^{-1}, respectively. A moderate increase in rate helps alleviate the stress concentration and thus inhibits microcrack formation in the powder compact. In contrast, a slower release rate allows gradual stress relaxation, reducing

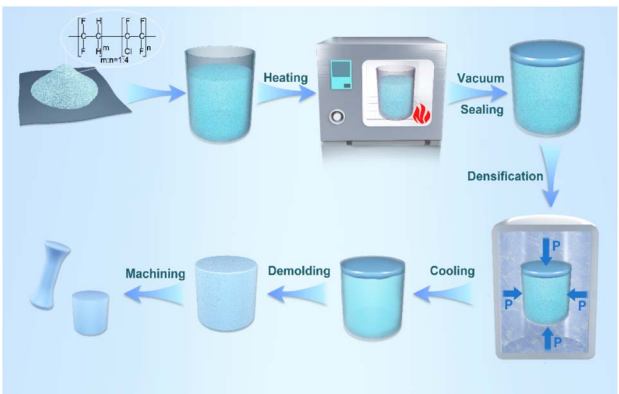

Fig. 1 Schematic illustration of isostatic pressing for F2314.

the risk of damage during unloading. After pressing, the sample was cooled to room temperature within the equipment, then demolded. Finally, mechanical machining was used to obtain samples with specific dimensions for various characterizations. At least three independent specimens were prepared for each compaction temperature condition.

Characterization methods

Thermal characterization. The mobility of the molecular chains in the F2314 powder at different temperatures was characterized *in situ* using a VTMR-20-010V-I NMR analyzer (Suzhou Niumag Analytical Instrument Co., Ltd). The transverse relaxation time (T_2) was measured *via* the magic sandwich echo-free induction decay (MSE-FID) pulse sequence with the following parameters: relaxation delay of 4000 ms, 32 scans, and a sampling frequency of 333.33 kHz.

The thermal transitions of both the raw powder and the pressed samples were analyzed using a Mettler DSC30 (Mettler-Toledo International Inc., Germany). The samples (~10 mg) were sealed in aluminum crucibles. Under a nitrogen atmosphere (20 mL min^{-1}), the thermal program involved cooling from room temperature to 0 °C at 10 °C min^{-1}, followed by heating to 150 °C at the same rate.

Structural characterization. *In situ* high-temperature XRD patterns of the F2314 powder and *ex situ* patterns of the pressed samples were acquired using a Bruker D8 Discover diffractometer (Bruker AXS GmbH, Germany) with Cu Kα radiation. For *in situ* tests, the temperature was varied from room temperature to 140 °C at a heating rate of 10 °C min^{-1}, with diffraction patterns collected at specific temperatures. The diffraction angle (2θ) range was 10–60° with a step size of 0.01°. The internal defect structure of the isostatically pressed samples was examined using a CD-300BX/μCT system (Chongqing ZhenCe Technology Co., Ltd). Samples with dimensions of Φ20 mm × 6 mm were scanned at 150 kV, 200 μA, and a voxel resolution of 17 μm.

The morphological features of the fracture surfaces of the pressed samples (after cryo-fracturing in liquid nitrogen) were observed using an SEM 5000 microscope (Guoyi Quantum Technology Co., Ltd) at an accelerating voltage of 10 kV. Prior to observation, the surfaces were sputter-coated with a thin gold layer for 60 s.

Mechanical and physical characterization. The density of the pressed samples (Φ20 mm × 6 mm) was determined by the water displacement method using an ISAAS-02 H electronic balance (Sartorius, Germany) with a precision of 0.1 mg. Industrial distilled water (pH 6.0–7.5, conductivity ≤0.1 μS cm^{-1}) was used as the medium. Each reported value represents the average of at least three measurements.

Dumbbell-shaped specimens (25 mm × 65 mm) were machined from the pressed samples and tested at room temperature using an Instron 5969 universal testing machine (Instron Corporation, USA). The tests were conducted with a gauge length of 15 mm and a crosshead speed of 5 mm min^{-1}. A minimum of three specimens were tested for each condition.

The viscoelastic properties of the pressed samples (30 mm × 10 mm × 1.5 mm) were characterized using a DMA 242C analyzer (NETZSCH, Germany) in three-point bending mode. The tests were performed at frequencies of 1, 2, 5, and 10 Hz with a constant amplitude of 60 μm and a static preload of 0.2 N. The temperature was first decreased from room temperature to 0 °C and then increased to 150 °C at a rate of 1 °C min^{-1}.

All quantitative data were obtained from at least three independent experiments and are presented as mean ± standard deviation. Statistical significance of differences between groups was determined using one-way analysis of variance (ANOVA), with the significance level set at $p < 0.05$. Post hoc tests were performed for multiple comparisons where applicable.

Results and discussion

Molecular chain motion behavior

LF-NMR, which is a powerful tool for probing the mobility of polymer chains, measures the transverse relaxation time (T_2) of protons.[27–30] A longer value indicated enhanced segmental mobility within the polymer. The magnetization decay curves and the corresponding relaxation times for F2314 at various temperatures are presented in Fig. 2.

As shown in Fig. 2(b), the T_2 value gradually increased by 15.4% from 201 to 232 μs when the temperature rose from 65 to 95 °C, suggesting progressively activated chain segment motion

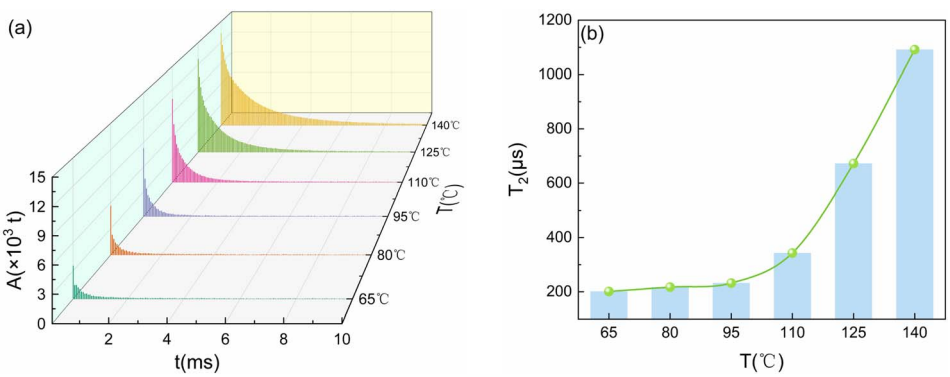

Fig. 2 For F2314 at various temperatures: (a) MSE-FID decays and (b) the corresponding T_2 values.

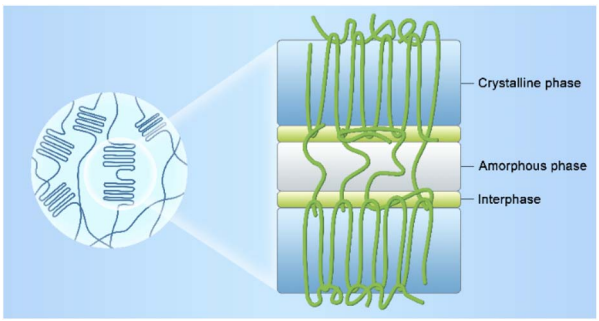

Fig. 3 Schematic depiction of the semicrystalline polymer structure.

in the amorphous regions. The T_2 value significantly increased to 343 μs at 110 °C, a 47.8% increase compared with its value at 95 °C. This increase signifies substantially enhanced molecular chain mobility. Furthermore, the T_2 value increased sharply to 672 μs and 1091 μs at 125 °C and 140 °C, respectively. This dramatic increase underscored the high-temperature sensitivity of the F2314 chain dynamics above 110 °C.

As schematically depicted in Fig. 3, the F2314 structure comprises crystalline, amorphous, and interfacial regions, as it is a semicrystalline polymer.[31] The "rigid" component in the LF-NMR analysis included the crystalline phase and segments in the amorphous region that were restricted at the measurement temperature.

The phase composition was quantitatively analyzed by fitting the magnetization decay data using a three-component model based on eqn (1) and (2),[24] which accounted for the signal contributions from rigid chains, the mobile amorphous phase, and the interface phase.

$$A(t) = A_1 \exp\left[-\left(\frac{t}{T_1}\right)^2\right] + A_2 \exp\left[-\left(\frac{t}{T_2}\right)^n\right] + A_3 \exp\left[-\left(\frac{t}{T_3}\right)^2\right] \quad (1)$$

$$\chi_1 = \frac{A_1}{A_1 + A_2 + A_3} \quad (2)$$

here, $A(t)$ represents the magnetization intensity at time t. A_1, A_2, and A_3 represent the initial signal intensities of the rigid, amorphous, and interfacial components, respectively. T_1, T_2, and T_3 are the relaxation times corresponding to the rigid, amorphous, and interfacial components, respectively. The signaling components of the hard, soft, and intermediate phases of polymer F2314 at different temperatures were obtained by fitting the decay spectra of the magnetization vector from the low-field nuclear magnetic resonance test *via* eqn (1), as shown in Fig. 4.

The magnetization vector decay spectrum showed a good fit with eqn (1) within the 65–140 °C test temperature range, with the fitting correlation coefficient exceeding 0.99. As summarized in Fig. 5 and calculated using eqn (2), the proportion of rigid segments (χ_1) exhibited a marked nonlinear decrease with increasing temperature, with their proportion decreasing from 30.17% at 65 °C to 22.99% at 95 °C, followed by a sharp decline to 8.32% at 110 °C. Notably, the rigid segments were completely absent at 125 and 140 °C, indicating the complete transformation of the molecular chains into a mobile, random coil conformation. Consequently, this trend provides direct evidence of the intrinsic link between microscopic chain mobility and thermal energy.

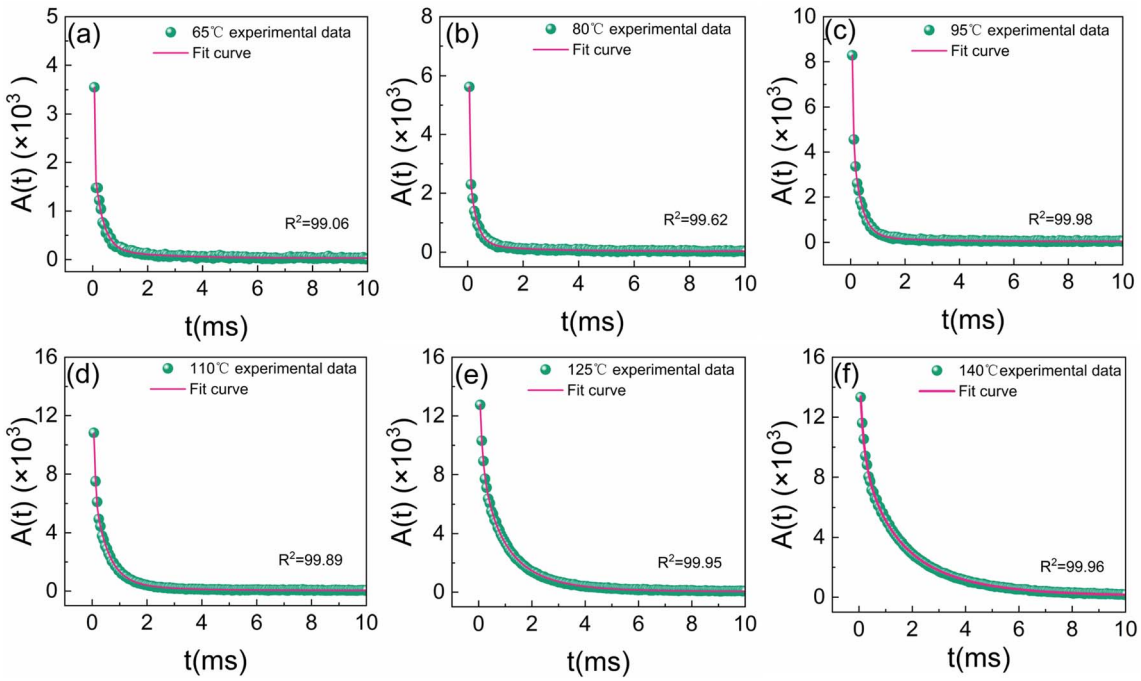

Fig. 4 Nonlinear fitting of the MSE-FID decay of F2314 at various temperatures.

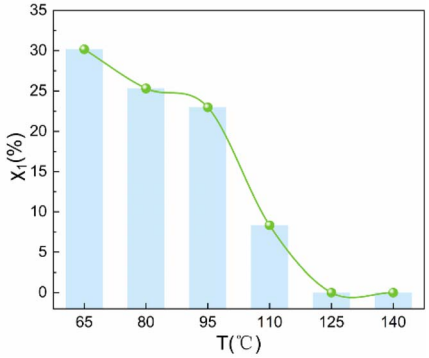

Fig. 5 The temperature variation law of the rigid segments of F2314. Amorphous halos at 125 and 140 °C, confirming the complete melting.

Crystallization performance evolution

DSC analysis. The thermal behavior of F2314 was first investigated using DSC. As presented in the DSC heating curve of the raw F2314 powder in Fig. 6(a), the two primary thermal events were as follows: the glass transition temperature (T_g) of the amorphous phase was 40.3 °C (onset at 36.2 °C and endset at 60.7 °C), and the melting endotherm (T_m) had a peak at 121.1 °C (onset at 103.0 °C and endset at 137.5 °C).

The melting behavior of the specimens compacted at different temperatures varied significantly, as depicted in Fig. 6(b). The specimens pressed at 65, 80, and 95 °C exhibited broad and weak melting endotherms similar to those of the raw material, indicating that the material had no significant melting-recrystallization during pressing below its T_m. In contrast, the sample compacted at 110 °C had no discernible melting peak. This phenomenon can be interpreted within the framework of pressure-influenced crystallization kinetics. At 110 °C under 100 MPa isostatic pressure, chain mobility is enhanced for densification but may still be restricted for the development of well-ordered, stable crystals. The applied pressure could promote the formation of metastable or imperfect crystalline domains. During the subsequent DSC heating scan at ambient pressure, these pressure-formed domains may reorganize or undergo melt-recrystallization at temperatures overlapping with other thermal events, leading to a broad, undetectable melting endotherm. Interestingly, the sample pressed at 125 °C presented a distinct melting peak at 114.0 °C. This temperature was likely near the optimal crystallization temperature, which provided sufficient chain mobility to develop a relatively well-ordered crystalline phase. The melting peak vanished again for the sample pressed at 140 °C, which could be attributed to the excessive thermal energy hindering crystal nucleation and growth, resulting in low crystallinity upon cooling.

XRD analysis. The evolution of the crystal structure was directly probed using *in situ* high-temperature X-ray diffraction (XRD). The XRD patterns of the raw F2314 powder acquired at elevated temperatures are shown in Fig. 7(a). The three distinct diffraction peaks at 16.2°, 16.5°, and 17.2° at room temperature corresponded to the (101), (102), and (103) crystal planes of polychlorotrifluoroethylene (PCTFE), respectively.[24,25,32] These peaks essentially remained unchanged at 65 and 80 °C. Upon heating to 95 and 110 °C, the (101) and (102) crystal planes persisted, but the (103) crystal plane disappeared, indicating the melting or phase transformation of the less perfect microcrystals associated with this plane. All the crystalline diffraction peaks transformed into broad amorphous halos at 125 and 140 °C, confirming the complete melting.of the crystalline phase and aligning with the DSC results.

As shown in the XRD patterns of the compacted samples in Fig. 7(b), the diffraction peak positions were consistent with those of the raw material, but their intensities generally decreased with increasing compaction temperature, suggesting reduced overall crystallinity. The samples pressed at 110, 125, and 140 °C had similar diffraction intensities, which highlighted that the intensity of the DSC melting endotherm could more effectively characterize the degree of crystallinity, but XRD had limitations in discerning it.[33–35]

Crystallinity analysis. The crystallinity (χ_c) was quantified using DSC and XRD for a comprehensive comparison. From the DSC, χ_c was calculated using eqn (3).[33]

$$\chi_c = \frac{\Delta H_m}{\Delta H_m^0} \quad (3)$$

where $\triangle H_m$ and $\triangle H_m^0$ (43.5 J g^{-1}) represent the melting enthalpy of the sample and 100% crystalline PCTFE,

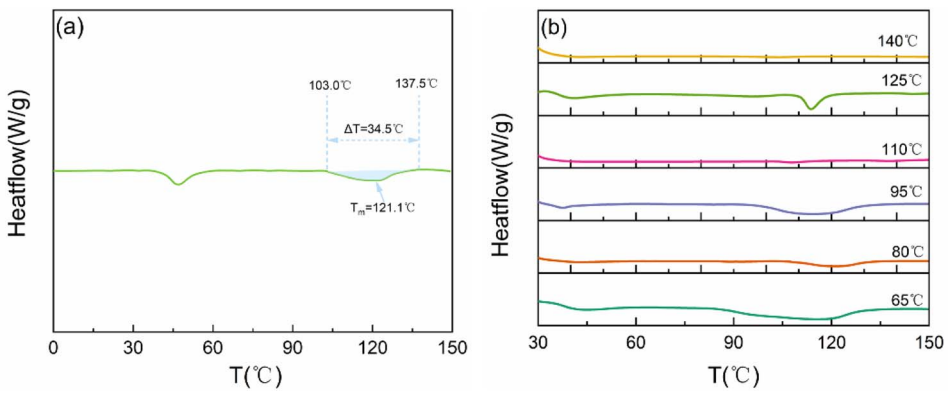

Fig. 6 DSC curves of F2314 (a) heated and (b) compacted at various temperatures.

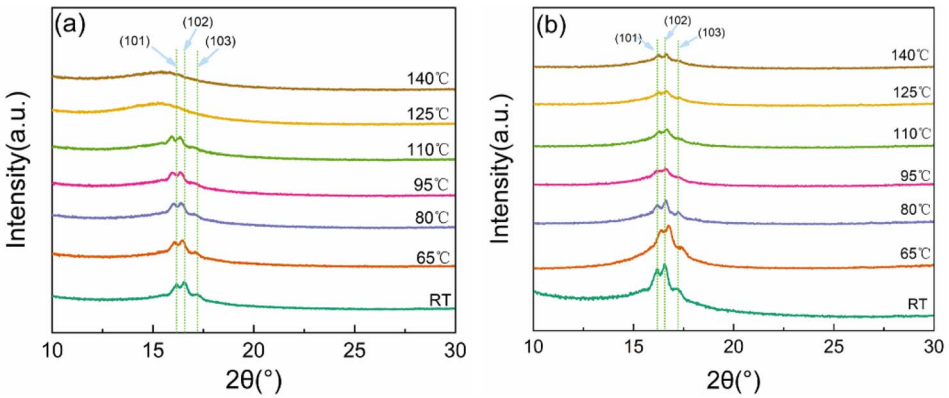

Fig. 7 XRD patterns of F2314 (a) heated and (b) compacted at various temperatures.

respectively.[36] The melting peak integration for the raw material is illustrated in Fig. 8(a).

From XRD, χ_c was determined using eqn (4).

$$\chi_c = \frac{I_c}{I_c + I_a} \quad (4)$$

where I_c and I_a represent the integrated areas of the crystalline and amorphous regions, respectively. A representative peak fit for the raw material is shown in Fig. 8(b).

The *in situ* XRD-calculated crystallinity of the F2314 powder increased from 6.49% at room temperature to 7.81% at 80 °C, then decreased to 5.98% at 110 °C, and finally decreased to zero at 125 and 140 °C (Fig. 8(c)). This non-monotonic trend indicated competition between thermally induced crystallization at lower temperatures and crystal melting/destruction at higher temperatures.

As summarized in the comparative analysis of the crystallinity of the compacted samples in Fig. 8(d), DSC and XRD consistently revealed a trend of initial increase followed by a decrease with increasing compaction temperature. The samples pressed at 80–95 °C had the highest crystallinity values, which decreased at higher temperatures. This trend underscored the profound influence of the thermal history during pressing. At lower temperatures (65–95 °C), the combined effect

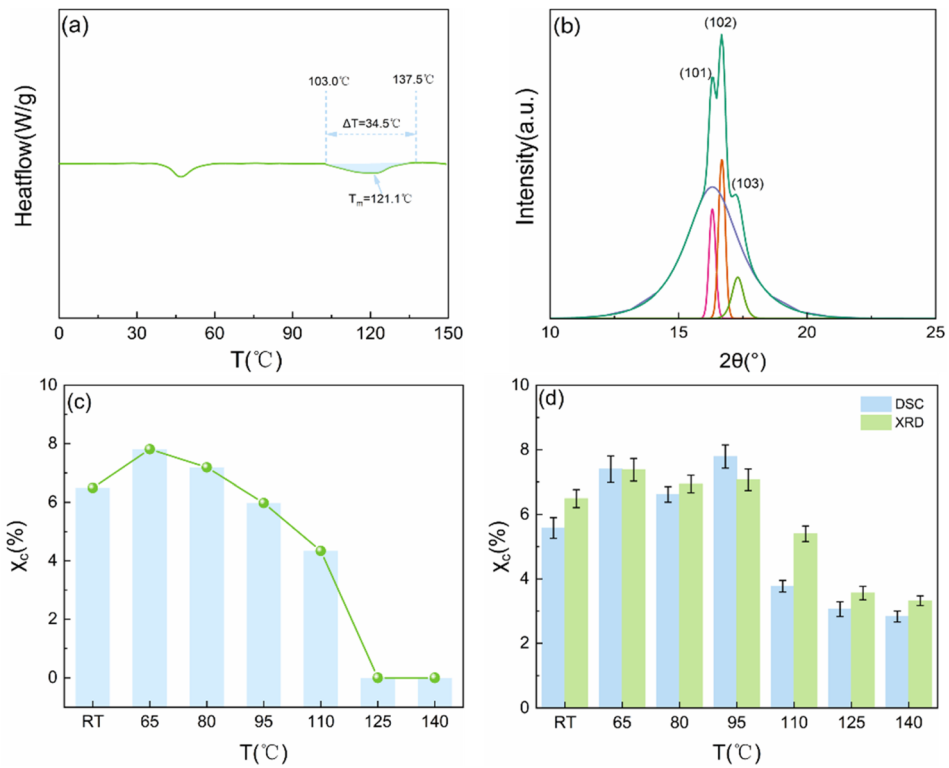

Fig. 8 Crystallization behavior of F2314 heated and compacted at various temperatures. For the F2314 raw material, (a) DSC analysis, (b) XRD peak fitting results, and (c) crystallinity at various temperatures were determined using *in situ* XRD. (d) Crystallinity of F2314 compacted at various temperatures, as determined *via* XRD and DSC analysis.

of enhanced chain mobility and applied pressure promoted segmental rearrangement and crystallization. In contrast, the increased thermal motion at temperatures above 95 °C disrupted the formation of stable crystal nuclei, resulting in lower final crystallinity.

Microstructure and evolution of forming density

Analysis of internal defects *via* X-ray industrial CT. The internal quality and defect distribution of the pressed specimens were visualized using X-ray industrial CT, which is a non-destructive method. As shown in the CT images of the F2314 specimens compacted at different temperatures in Fig. 9, densification improved dramatically with increasing temperature.

The sample pressed at 65 °C had a loose, porous structure with numerous, uniformly distributed fine pores, indicating poor cohesion between the original powder particles (Fig. 9(a)). The internal void content decreased at 80 °C, and the porous state transitioned from being widespread to localized (Fig. 9(b)). A critical change occurred at 95 °C, where the sample achieved near-full densification, with only a few isolated pores remaining near the edges (Fig. 9(c)). As shown in Fig. 9(d–f), the specimens were almost completely dense when the compaction temperature reached 110–140 °C, with no observable pores either at the center or the edges. The isotropic nature of the internal quality of these high-temperature specimens underscored the fundamental advantage of isostatic pressing, with the uniform transfer of pressure in all directions enabling three-dimensional homogeneous compaction.[37,38]

Analysis of the fracture morphology using SEM. As presented in Fig. 10, the fracture surfaces of the cryogenically fractured specimens were examined using SEM to gain insights into the interfacial bonding at the microscopic level. The morphology evolution correlated strongly with the CT observations.

At 65 °C, the boundaries between the original F2314 particles were clearly discernible, with the fracture surface exhibiting a highly porous structure and numerous interconnected pores, consistent with the observed low density (Fig. 10(a)). The morphological characteristics showed limited improvement when the temperature was increased to 80 °C, and a porous network similar to that at 65 °C was retained (Fig. 10(b)). Notably, enhanced interfacial bonding emerged at 95 °C, where the previously continuous large-area pores were largely eliminated, accompanied by a marked increase in the material density and blurred interparticle boundaries (Fig. 10(c)). The fracture surface developed a stepped morphology at 110 °C, with only a few residual pores, indicating further progress in particle fusion (Fig. 10(d)). The sample pressed at 125 °C showed completely fused particle interfaces, yielding a relatively smooth surface with river-like patterns (Fig. 10(e)). Interestingly, the fracture surface became even denser and smoother at 140 °C, yet exhibited numerous radial bands, characteristic of brittle fracture behavior (Fig. 10(f)).

Density and relative density of specimens. The quantitative evolution of densification was characterized using density measurements, and the results are summarized in Fig. 11. The absolute density increased from 1.824 g cm^{-3} at 65 °C to 2.040 g cm^{-3} at 95 °C, followed by stabilization at about

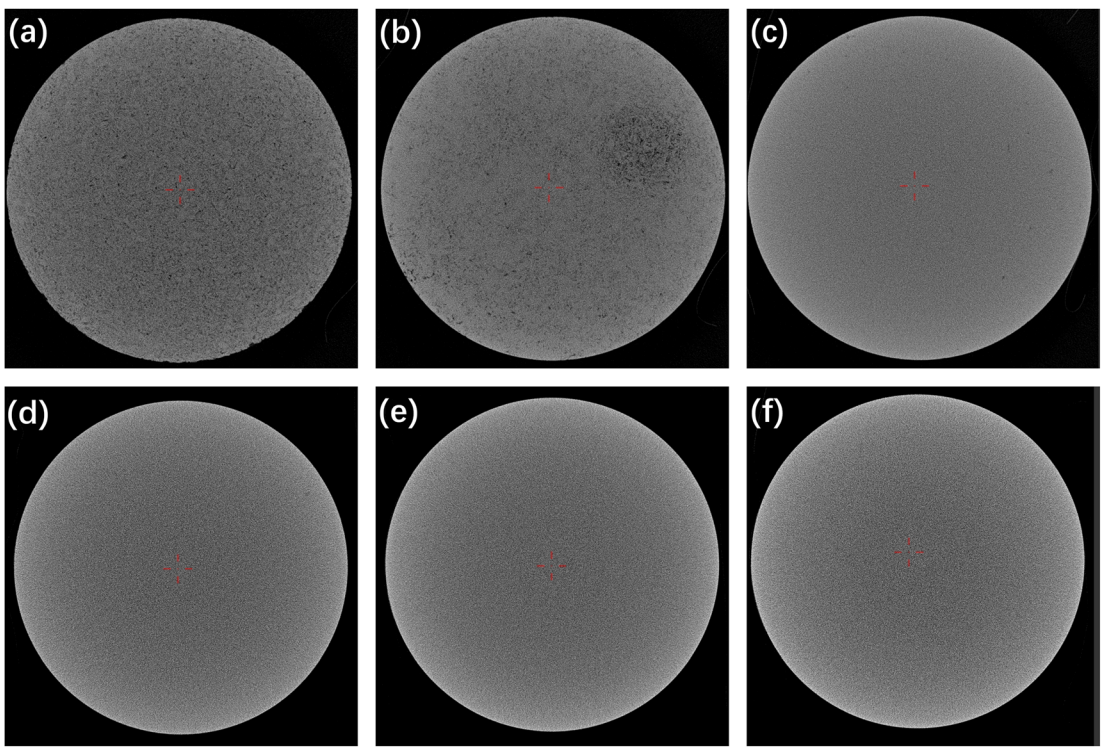

Fig. 9 CT images of the F2314 specimens compacted at temperatures of (a) 65, (b) 80, (c) 95, (d) 110, (e) 125, and (f) 140 °C.

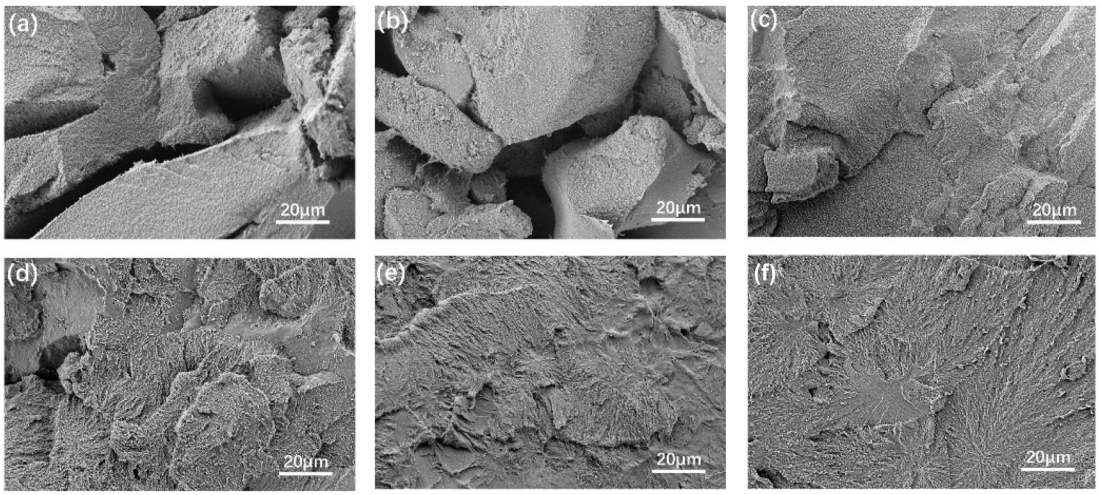

Fig. 10 SEM images of the brittle fracture cross-sections of F2314 compacted at compaction temperatures of (a) 65, (b) 80, (c) 95, (d) 110, (e) 125, and (f) 140 °C.

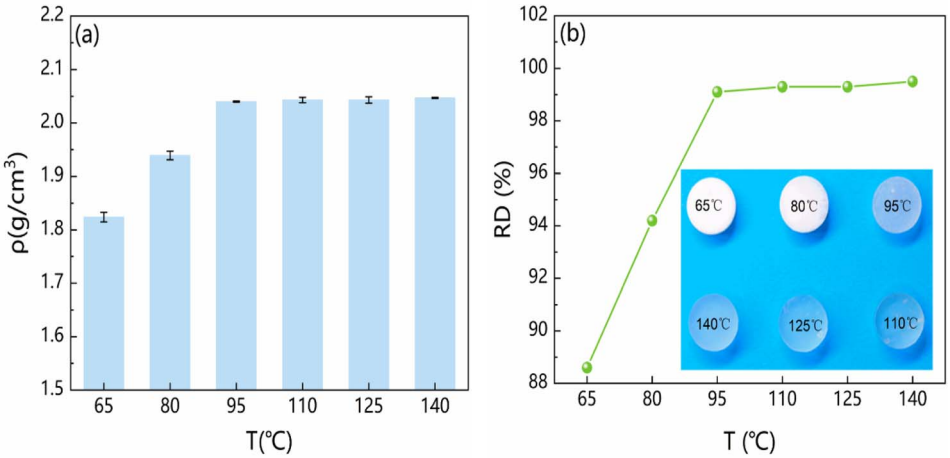

Fig. 11 Effects of the compaction temperature on (a) the forming density and (b) the relative density and appearance of F2314.

2.045 g cm^{-3} for temperatures between 110 and 140 °C (Fig. 11(a)).

As shown in Fig. 11(b), the relative density was calculated using the theoretical density of 2.0576 g cm^{-3} for F2314.[22] The relative density rose rapidly from 88.6% to 99.1% as the compaction temperature increased from 65 to 95 °C. The relative density exceeded 99% above 95 °C, with the rate of increase slowing considerably and reaching a maximum of 99.5% at 140 °C. As shown in the inset in Fig. 11(b), the macroscopic appearance of the samples transitioned from white and opaque at low temperatures to transparent at high temperatures. This visual change was a direct manifestation of reduced light-scattering centers (pores and interfaces), further corroborating the enhanced densification.

In summary, CT, SEM, and density measurements yielded highly consistent results, collectively reflecting the densification process of F2314 under isostatic pressing. The particles underwent primarily elastic deformation at lower temperatures (≤80 °C), resulting in weak interfacial bonding and a porous structure. As the temperature increased (≥95 °C), the mobility of the polymer chains increased, facilitating plastic deformation and pore filling, thereby significantly increasing the density and blurring particle boundaries. The sample density approached the theoretical limit when the temperature xceeded the critical value (~110 °C), and a well-fused, continuous matrix dominated the microstructure, with further increases in temperature yielding lower returns to densification.[39,40]

Tensile mechanical properties. The processing temperature was correlated with the macroscopic mechanical behavior by critically evaluating the tensile properties of isostatically pressed F2314 samples. As shown in the stress–strain curves and the derived mechanical parameters in Fig. 12, the compaction temperature had a profound influence on the deformation and failure mechanisms.

As shown in Fig. 12(a) and (b), the tensile response transitioned dramatically with increasing compaction temperature.

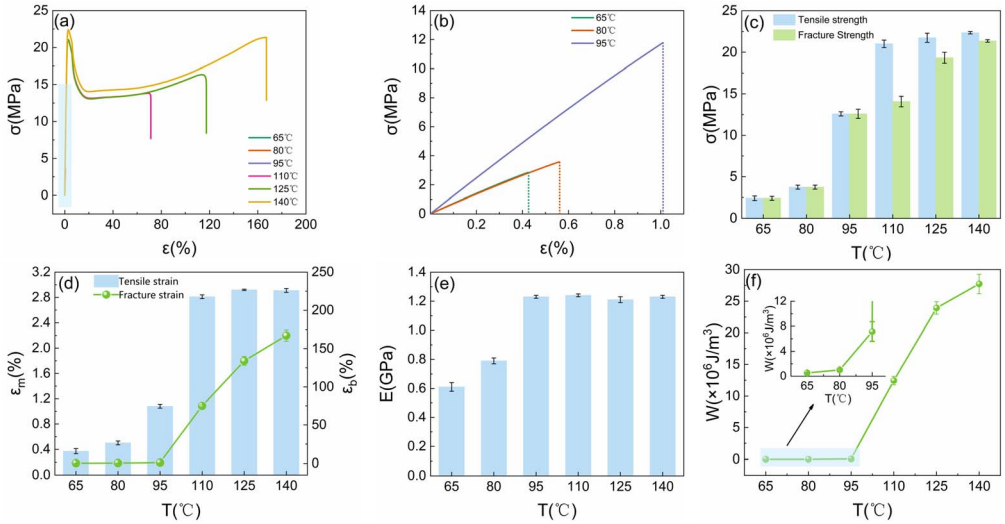

Fig. 12 Tensile mechanical properties of the F2314 specimens compacted at various compaction temperatures. (a) Stress–strain curves, (b) local magnification diagrams, (c) tensile strength and fracture strength, (d) tensile strain and fracture strain, (e) elastic modulus, and (f) fracture energy.

The specimens pressed at 65, 80, and 95 °C exhibited linear elastic behavior, followed by catastrophic fracture at low strains, a characteristic of brittle materials. In stark contrast, the specimens pressed at 110, 125, and 140 °C exhibited typical ductile behavior, which was characterized by a yield point, subsequent strain softening, and pronounced strain hardening before fracture.

The brittle-to-ductile transition is quantitatively detailed in Fig. 12(c) and (d). The tensile strength (taken as the fracture strength and yield strength for brittle and ductile specimens, respectively) increased from 2.41 MPa at 65 °C to 22.35 MPa at 140 °C, which was an increase of more than 9 times. More notably, the fracture strain (ε_b) experienced an extraordinary increase of more than 450 cycles, increasing from 0.37% at 65 °C to 167.10% at 140 °C. Consequently, this improved ductility was a direct result of enhanced interfacial bonding and a continuous, cohesive material structure formed at higher compaction temperatures. The observed brittle-to-ductile transition between 95 and 110 °C is a direct macroscopic consequence of the concurrent microstructural changes detailed in previous section. Within this critical temperature interval, the sharp decrease in rigid segment content (Fig. 5), the near-elimination of internal pores (Fig. 9), and the blurring/fusion of interparticle boundaries (Fig. 10) synergistically transformed the material from a weak, porous assembly of particles into a strong, cohesive continuum. This transformation fundamentally altered the failure mode from easy crack propagation along weak interfaces to extensive plastic deformation within a robust, interpenetrating network. In addition, the elongation at break is significantly correlated with the crystallinity. From 110 to 140 °C, the crystallinity of the isostatically pressed samples decreases monotonically with increasing temperature, weakening the rigidly ordered internal structure and significantly increasing elongation at break.

As presented in Fig. 12(e), the elastic modulus (E) is a measure of the material stiffness. E increased from 0.61 to about 1.23 GPa as the temperature rose from 65 to 95 °C, followed by stabilization within a narrow range of 1.21–1.24 GPa for temperatures ≥110 °C. This stabilization coincided with the achievement of a near-theoretical density (relative density >99%, as shown in Fig. 11), indicating that the intrinsic stiffness of the fully densified polymer matrix, rather than porosity, primarily governed the modulus.

The fracture energy density (w), a key toughness indicator, was calculated by integrating the area under the stress–strain curves (eqn (5)).[41,42] As shown in Fig. 12(f), w increased by several orders of magnitude, from 0.52×10^4 J m^{-3} at 65 °C to 2772.85×10^4 J m^{-3} at 140 °C. This dramatic increase underscores the superior ability of high-temperature pressed specimens to absorb energy and resist crack propagation.

$$w = \int_0^{\varepsilon_b} \sigma(\varepsilon)\mathrm{d}\varepsilon \tag{5}$$

The evolution of the mechanical properties was intrinsically linked to the microstructural changes detailed in previous section. The brittle failure at low temperatures (≤95 °C) stemmed from weak interfacial bonding and poor particle fusion, leading to easy propagation along particle boundaries. The ductile behavior observed at temperatures ≥ 110 °C was attributed to sufficient molecular chain interdiffusion across the particle interfaces, which formed a robust three-dimensional interpenetrating network. This network allowed for extensive plastic deformation through chain orientation and stretching before ultimate failure. The sample pressed at 125 °C showed an optimal combination of high strength and exceptional ductility, suggesting that this temperature facilitated the ideal balance between chain mobility (for interfacial healing) and microstructural development (for strength). In PBX applications, the binder's tough, ductile behavior was crucial for enhancing the crack resistance and overall structural integrity of the explosive components under mechanical or thermal

stress. A further increase in the temperature to 140 °C marginally improved ductility but did not significantly enhance strength and could introduce potential thermal risks, reinforcing 125 °C as the optimal processing condition.[43,44]

Viscoelasticity

Dynamic thermo-mechanical properties. To investigate the effect of compaction temperature on the molecular relaxation behavior of F2314, DMA was conducted on samples fabricated at 110–140 °C.

These samples exhibited macroscopic ductile fracture and high densification, indicative of a well-consolidated internal structure with minimal defects—features that enhance their representativeness for characterizing the material's bulk viscoelastic response. In contrast, the samples compacted at 65–95 °C exhibited incomplete densification, with a tendency for internal pore formation and interfacial defects. The dynamic mechanical behavior of these materials is significantly affected by structural heterogeneity, limiting accurate reflection of the intrinsic viscoelastic properties of the polymer matrix.

The spectra of the temperature-dependent storage modulus (E'), loss modulus (E''), and loss factor (tanδ) at various frequencies (1, 2, 5, and 10 Hz) are presented in Fig. 13.

The E'' and tan δ spectra showed a prominent relaxation peak within the 30–90 °C temperature range for all the samples, which was attributed to the glass-to-rubber transition of the amorphous phase in F2314. The material was in a glassy state below 30 °C, which was characterized by a high and relatively constant E' ($\approx$1.2 GPa), since the molecular chain segments were "frozen" with severely restricted mobility. The material underwent a glass transition above 30 °C. The chain segments gradually "thawed," leading to significantly increased mobility and a consequent rapid decrease in E'. The material entered the rubbery plateau above about 90 °C, where E' stabilized at a much lower value as the chains became highly mobile.

The test frequency notably affected the dynamic mechanical response. As shown in Fig. 13(a–f), an increase in the frequency from 1 to 10 Hz systematically shifted the E'' and tanδ peaks to higher temperatures, accompanied by an increase in their peak intensities. This frequency dependence was a hallmark of viscoelastic behavior. At higher frequencies, the material exhibited greater rigidity (higher E'), and the observed glass transition was delayed to a higher temperature since the polymer chain segments could not relax and responded promptly to the applied oscillatory stress.[45–48] Concurrently, the intensified internal friction between molecules led to greater energy dissipation, manifesting as increased E'' and tanδ peak values.

The T_g value, which was identified from the peak maximum of tan δ, and its corresponding tanδ peak values are summarized in Table 1 for all conditions. Notably, at any given frequency, the specimens pressed at different temperatures had remarkably consistent T_g values (*e.g.*, 53.0–53.3 °C at 1 Hz). This indicated that the global segmental mobility governing the glass transition was largely independent of the isostatic compaction temperature when a fully densified, well-fused structure was achieved above 110 °C.

Activation energy of the glass transition. The magnitude of the apparent activation energy (ΔE) for the glass transition reflected the energy barrier that the polymer chains had to overcome to initiate coordinated segmental motion. The kinetic behavior followed the Arrhenius equation (eqn (6)).[48]

$$\omega = \omega_0 \exp\left(-\frac{\Delta E}{RT_g}\right) \quad (6)$$

Table 1 T_g and tan δ_{peak} for the F2314 specimens under different compaction temperatures at various test frequencies

	T_g (°C)			Tan δ_{peak}		
f (Hz)	110 °C	125 °C	140 °C	110 °C	125 °C	140 °C
1	53.0	52.6	53.3	0.551	0.619	0.646
2	55.5	55.3	55.8	0.564	0.631	0.664
5	57.5	58.7	59.3	0.574	0.649	0.686
10	60.8	61.6	61.8	0.585	0.666	0.702

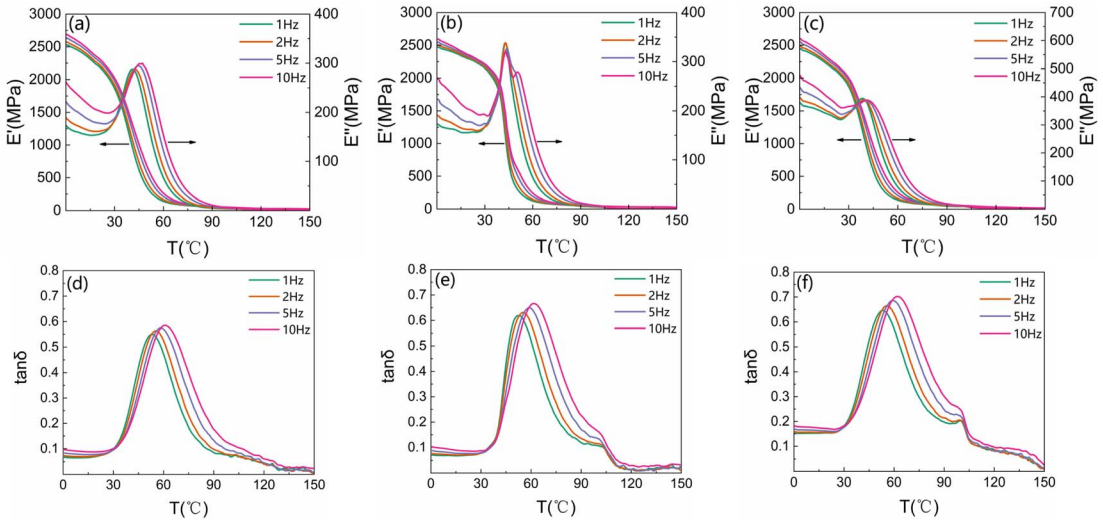

Fig. 13 Dynamic mechanical temperature spectra of F2314 at compaction temperatures of (a and d) 110, (b and e) 125, and (c and f) 140 °C.

here, ω, ω_0, ΔE, T_g, and R represent the angular frequency (in rad s^{-1}), the pre-exponential factor (in rad s^{-1}), the activation energy of the glass transition (in kJ mol^{-1}), the glass transition temperature (in K), and the gas constant (=8.314 J mol^{-1} K^{-1}), respectively.

The relationship between ω in eqn (6) and the test frequency (f (Hz)) is given by eqn (7).

$$\omega = 2\pi f \tag{7}$$

Furthermore, taking the logarithm of eqn (6) yields eqn (8).

$$\mathrm{Ln}\ \omega = \ln\ \omega_0 - \frac{\Delta E}{RT_g} \tag{8}$$

As shown in Fig. 14, ΔE was determined from the slope of the linear plot of ln (ω) *versus* $1/T_g$. The ΔE values calculated at 110, 125, and 140 °C were 275.3, 233.5, and 245.1 kJ mol^{-1}, respectively. All the fitting correlation coefficients (R^2) exceeded 0.99, indicating excellent linearity of the data. The ΔE value was in close agreement with the value of 244.3 kJ mol^{-1} reported by Song *et al.*,[49] thereby further confirming the reliability of the experimental results.

The ΔE values fell within a relatively narrow range of 233.5–275.3 kJ mol^{-1} and showed no systematic trend with compaction temperature. This further confirmed the fundamental dynamics of the glass transition. Thus, the bulk viscoelastic properties of the well-consolidated F2314 were insensitive to the isostatic compaction temperature within the high-temperature regime (110–140 °C). The slight variations were likely within experimental error and may have been influenced by subtle differences in the final amorphous structure or residual thermal history. The observed consistency in viscoelasticity underpinned the stability of the mechanical properties of the samples molded above the critical temperature of 110 °C, as detailed in previous section.

Isostatic pressing densification mechanism. The intrinsic mechanism governing the temperature-dependent densification of F2314 during isostatic pressing was elucidated by synthesizing comprehensive experimental evidence. A distinct evolutionary pathway, which transitioned from incomplete particle consolidation to the formation of a fully homogenous structure, characterized this process (Fig. 15). The temperature exceeded T_g at lower temperatures (65–95 °C), but the molecular chain mobility was restricted, and the crystalline phase was largely preserved. Consequently, densification relies predominantly on the elastic deformation and mechanical interlocking of powder particles, with minimal interdiffusion of chains across interfaces. This resulted in weak interfacial bonding, significant porosity, and brittle fracture behavior, as clearly evidenced by the CT and SEM analyses.

The mechanism showed a critical shift as the compaction temperature entered an intermediate range, culminating at about 110 °C. The increased thermal energy significantly increased the mobility of chain segments, initiating the melting of imperfect crystallites. This facilitated a transition from mere mechanical interlocking to a combined mechanism in which interfacial healing through chain interdiffusion played a dominant role. The markedly improved density and the consequent shift from brittle to ductile fracture underscored the importance of this transitional stage. The crystalline phase completely melted upon entering the high-temperature regime (125–140 °C), thereby providing the maximum mobility of the molecular chains. Thereafter, extensive plastic flow and profound interdiffusion dominated densification, eradicating the original particle boundaries and forming a dense, three-dimensional interpenetrating network. Consequently, this yielded a near-theoretical density and superior mechanical properties, including high strength and exceptional toughness. It is important to recognize that the thermomechanical history of the material extends beyond the pressing stage. Thermomechanical analysis (TMA) results indicate that within the pressing temperature range studied in this work (above 95 °C), the F2314 material does not exhibit significant additional thermal expansion behavior (as seen from Fig. S2). This suggests that after pressing at the optimal temperature of 125 °C, no appreciable additional volumetric contraction due to CTE occurs during the subsequent cooling stage. Therefore, the selection of this temperature primarily ensures complete crystal

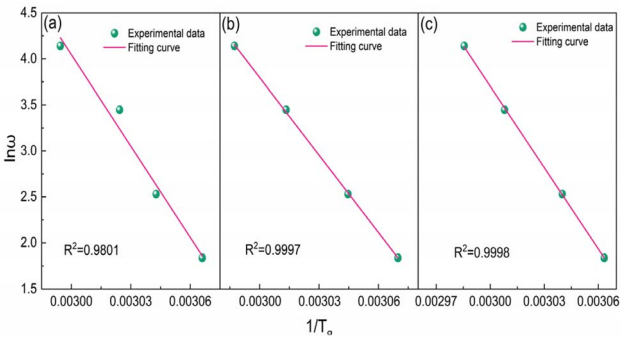

Fig. 14 Ln $\omega - 1/T_g$ curves of F2314 at compaction temperatures of (a) 110, (b) 125, and (c) 140 °C.

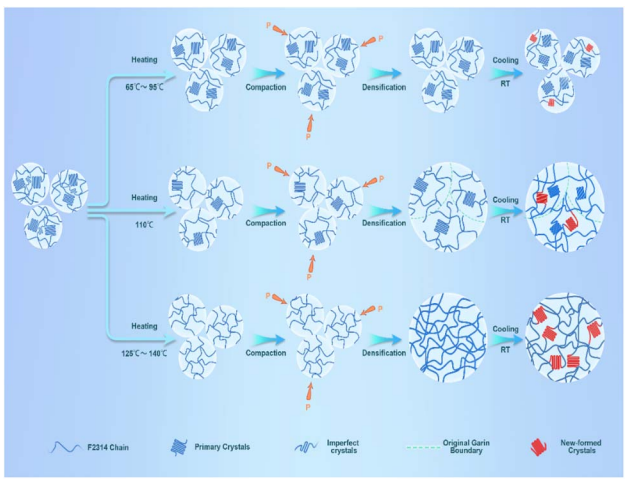

Fig. 15 Schematic depiction of isostatic pressing for the raw F2314 materials at various temperatures.

melting and sufficient chain interdiffusion, thereby forming a robust interpenetrating network to achieve high density and excellent performance.

This mechanistic understanding provides a scientific basis for process optimization. The optimal temperature for the isostatic pressing of F2314 was 125 °C. This approach ensured complete crystal melting and sufficient chain interdiffusion to form a robust interpenetrating network, achieving the desired high performance. This temperature also represents a balanced choice considering the CTE-related behavior, helping to coordinate the thermal contraction effects during cooling. Conversely, a higher temperature of 140 °C could offer marginal gains in ductility but provided no significant advantage in strength and increased the thermal risk profile, a critical consideration for PBX processing. Therefore, 125 °C represented the optimal compromise, which achieved an ideal balance between mechanical performance and operational safety to enable the high-quality manufacturing of F2314-based PBX components. Addtionally,it should be noted that the densification process of F2314 during isostatic pressing is fundamentally physical in nature, involving no formation or cleavage of chemical bonds (as seen from Fig. S3). This study elucidates the densification mechanism of F2314 and systematically compares its high-temperature compaction behavior with that of short-chain polymers and non-polymeric materials—including metallic and ceramic powders. For polymeric systems, low molecular weight facilitates void filling owing to reduced melt viscosity and enhanced melt fluidity; however, it compromises structural integrity due to insufficient chain entanglement. In contrast, high molecular weight polymers exhibit superior densification, attributable to increased chain mobility and a more robust, percolating entanglement network.[50] Non-polymeric materials, lacking both chain entanglement and polymer-chain diffusion, densify exclusively through solid-state mechanisms—namely, particle rearrangement, plastic deformation under load, and thermally activated sintering diffusion.[51]

Conclusion

This study systematically elucidated the intrinsic correlation between the isostatic compaction temperature and the microstructure-property evolution of the F2314 binder for PBX applications. The densification mechanism fundamentally transitions from particle-level mechanical interlocking at low temperatures (65–95 °C) to molecular-level chain interdiffusion and interpenetrating network formation at elevated temperatures (110–140 °C). The optimal compaction temperature of 125 °C achieved a critical balance, ensuring complete crystal melting and sufficient chain mobility to form a cohesive microstructure while maintaining process safety. Additionally, this temperature yielded F2314 samples with a near-theoretical density (>99.3%), an excellent tensile strength of 21.74 MPa, and an outstanding fracture toughness of 134% strain. These findings establish a scientific foundation for the high-quality manufacturing of F2314-based PBX components, which demonstrates that precise temperature control during isostatic pressing is crucial for achieving optimal mechanical properties and structural reliability in explosive formulations. Furthermore, the temperature-dependent relationship between the microstructure and performance revealed in this study provides a theoretical basis for the optimization of temperature parameters during isostatic pressing. By coordinating the optimal temperature window of 125 °C with key process parameters, including pressure, pressurization rate, and holding time, the overall performance of PBX components can be further enhanced. Notably, the significant technical challenges of conducting *in situ* measurements during isostatic pressing have led to uncertainties in precisely characterizing the evolution of F2314 crystallinity at high temperatures. Future studies incorporating more advanced *in situ* characterization techniques are expected to further enhance the understanding of the underlying microstructural transformation mechanisms. Notably, a key limitation of this study arises from the technical challenges of performing *in situ*, real-time microstructural characterization during the high-pressure, high-temperature isostatic pressing process. This introduces some uncertainty in precisely mapping the crystallinity evolution at elevated temperatures. Future studies incorporating more advanced *in situ* characterization techniques (*e.g.*, synchrotron X-ray imaging, high-pressure DSC) are expected to provide deeper insights into the real-time microstructural transformation mechanisms.

Author contributions

Baogang Yang: writing – original draft, formal analysis, visualization, conceptualization. Kai Yang: investigation. Zhijian Yang: writing – review & editing, validation. Kezhen Lv: funding acquisition. Haiying Yang: formal analysis. Jiang Li: supervision. Shaoyun Guo: project administration.

Conflicts of interest

The authors declare that they have no known competing financial interests or personal relationships that could influence the work reported in this paper.

Data availability

The data that support the findings of this study are available from the corresponding author upon reasonable request.

Supplementary information (SI): raw material morphology, thermomechanical analysis and infrared spectroscopy analysis. See DOI: https://doi.org/10.1039/d5ra09872f.

Acknowledgements

This work was supported by the National Natural Science Foundation of China (Grant No. 12272360) and the Disciplinary Fund of the Institute of Chemical Materials (Grant No. SXK-2021-14), CAEP.

References

1 G. Shen, C. Chen, K. Li, X. Wang, Z. Cui, J. Wu, K. Liang, X. Cui, Y. Bu, Y. Li, Y. Niu and H. Nan, *FirePhysChem*, 2026, **6**, 28–34.

2 T. Rotariu, A. E. Moldovan, G. Toader, A. Diacon, E. Rusen, R. E. Ginghina, O. Iorga, H. R. Botiș and T. Klapötke, *Polymers*, 2023, **15**, 1790.

3 H. Guo, J. Luo, P. Shi and J. Xu, *Def. Technol.*, 2014, **10**, 154–160.

4 Y. Bu, C. Chen, F. Jiang, X. Wang, D. Che and H. Nan, *Propellants, Explos., Pyrotech.*, 2022, **47**, e202200093.

5 C. Zeng, C. Lin, Z. Yang, G. He, S. Zheng, F. Gong and F. Nie, *Def. Technol.*, 2025, **54**, 89–106.

6 X. Li, X. Xiong, K. Song, J. Liu, L. Bai, J. Chen, J. Chen, X. Tu, Y. Yin and D. Liu, *Chin. J. Polym. Sci.*, 2025, **43**, 1651–1660.

7 S. Ge, W. Zhang, J. Sang, S. Yuan, G. V. Lo and Y. Dou, *Materials*, 2019, **12**, 3767.

8 G. He, P. Wang, R. Zhong, X. Li, H. Yin, J. Chen, S. Liu and Z. Yang, *Compos. Appl. Sci. Manuf.*, 2024, **177**, 107918.

9 J. Chen, F. He, Z. Liu, W. Hong, P. Wang, G. He and W. Yang, *Colloid Polym. Sci.*, 2025, **303**, 1423–1435.

10 X. Ji, D. Tang, Y. Li, Z. Xing, Y. Wang, L. Wang, Y. Gao and W. Qin, *Opt. Laser Technol.*, 2019, **120**, 105677.

11 Y. Guo, Y. Liu, J. Xie, J. Li, F. Wang, J. Lei, C. An, Z. Ma and B. Wu, *Def. Technol.*, 2025, **45**, 73–83.

12 P. Bao, J. Li, Z. Han, H. Ma and B. Wang, *FirePhysChem*, 2021, **1**, 139–145.

13 J. D. Yeager, A. M. Dattelbaum, E. B. Orler, D. F. Bahr and D. M. Dattelbaum, *J. Colloid Interface Sci.*, 2010, **352**, 535–541.

14 D. Graff Thompson and W. J. Wright, *AIP Conf. Proc.*, 2004, **706**, 503–506.

15 H. Sun, X. Fan, M. Zhan, J. Guo and J. Zhang, *Int. J. Mech. Sci.*, 2024, **282**, 109683.

16 K. Lv, K. Yang, B. Zhou, F. Zhang, J. Guo, C. Han and Y. Tian, *Mater. Des.*, 2021, **207**, 109872.

17 Y. Xu, Y. Tian, H. Wang, C. Zhang, C. Liu, Z. Yang, W. Zhang, R. Liu and P. Chen, *Powder Technol.*, 2023, **413**, 118044.

18 U. M. Attia, *Crit. Rev. Solid State Mater. Sci.*, 2021, **46**, 587–610.

19 J. Li, Y. Ji, J. Chang, N. Tian, L. Song, L. Chen and L. Li, *Polymer*, 2017, **119**, 107–111.

20 J. Chang, Y. Lin, W. Chen, F. Tian, P. Chen, J. Zhao and L. Li, *J. Polym. Sci., Part B: Polym. Phys.*, 2019, **57**, 607–620.

21 Y. Yang, M. Zhu, Z. Shao, X. Cao, L. Huang, J. Zhu, Y. Li, X. Zhao, S. Li, C. Zhu and Y. Liu, *Appl. Surf. Sci.*, 2025, **697**, 163033.

22 C. Deng, H. Liu, Y. Cui, X. Zhu, Y. Bai and Z. Hu, *Polymer*, 2023, **264**, 125562.

23 G. He, X. Li, Y. Jiang, Y. Dai, R. Xu, C. Zeng, X. Tu and Z. Yang, *J. Mater. Sci.*, 2020, **55**, 15726–15740.

24 Z. Wu, X. He, C. Zhu, J. Xu, H. Yong and X. Zhao, *Polym. Test.*, 2024, **141**, 108654.

25 Y. Xiao, Y. Bao, Y. Liu, J. Xu, A. Zhang, C. Zhu and S. Cui, *Macromol. Chem. Phys.*, 2022, **223**, 2100469.

26 H. Qi, Z. Liu, X. Zhou, Y. Yang, Z. Shao, T. Ren, J. Xu and Z. Li, *Surf. Interfaces*, 2025, **62**, 106297.

27 V. Räntzsch, M. Haas, M. B. Özen, K. F. Ratzsch, K. Riazi, S. Kauffmann-Weiss, J. K. Palacios, A. J. Müller, I. Vittorias, G. Guthausen and M. Wilhelm, *Polymer*, 2018, **145**, 162–173.

28 D. M. DeLongchamp, K. L. Beers and C. L. Soles, *J. Polym. Sci.*, 2022, **60**, 1021–1022.

29 J. Wang, Q. Guo, Z. Yao, N. Yin, S. Ren, Y. Li, S. Li, Y. Peng, J. Bai, B. Ning, J. Liang and Z. Gao, *Microchim. Acta*, 2020, **187**, 333.

30 T. Yamanobe, H. Uehara and M. Kakiage, in *Annual reports on NMR spectroscopy*, ed. G. A. Webb, Academic Press, 2010, 70, pp. 203–239.

31 R. H. Gee, L. E. Fried and R. C. Cook, *Macromolecules*, 2001, **34**, 3050–3059.

32 Z. Mencik, *J. Polym. Sci., Part B: Polym. Phys.*, 1973, **11**, 1585–1599.

33 M. Doumeng, L. Makhlouf, F. Berthet, O. Marsan, K. Delbé, J. Denape and F. Chabert, *Polym. Test.*, 2021, **93**, 106878.

34 R. Zhang, Y. Xu, A. Lu, K. Cheng, Y. Huang and Z. Li, *Polymer*, 2008, **49**, 2604–2613.

35 A. K. Pathak and T. Yokozeki, *J. Compos. Sci.*, 2022, **6**, 332.

36 D. M. Hoffman, F. M. Matthews and C. O. Pruneda, *Thermochim. Acta*, 1989, **156**, 365–372.

37 X. Zhang, Y. Zheng, D. Wang and F. Zhou, *Nano Energy*, 2017, **40**, 95–106.

38 J. Duffy, N. Norberg, J. Dawes and M. Taylor, Lyon, France, 2022.

39 S. J. Park, D. H. Kim, H. G. Ju, S. J. Park, S. Hong, Y. Son and I. H. Ahn, *J. Mater. Res. Technol.*, 2023, **25**, 3610–3623.

40 S. J. Park, S. J. Park, Y. Son and I. H. Ahn, *Addit. Manuf.*, 2022, **55**, 102841.

41 H. Liu, L. Chen, Y. Peng, X. Li, H. Zhang, Y. Chen, Z. Li and F. Dai, *Cellulose*, 2024, **31**, 8169–8187.

42 X. Zhang, W. Liu, D. Yang and X. Qiu, *Adv. Funct. Mater.*, 2018, **29**, 1806912.

43 S. J. Park, J. W. Choi, S. J. Park, Y. Son and I. H. Ahn, *Mater. Des.*, 2022, **224**, 111417.

44 S. J. Park, H. G. Ju, S. J. Park, S. Hong, Y. Son and I. H. Ahn, *Mater. Des.*, 2023, **231**, 112045.

45 H. Zhuo, H. Wen, G. Liu, H. Chen and S. Chen, *Polymer*, 2018, **158**, 25–31.

46 K. Nitta, K. Ito and A. Ito, *Polymers*, 2023, **15**, 3590.

47 J. Rieger, *Polym. Test.*, 2001, **20**, 199.

48 C. A. Gracia-Fernández, S. Gómez-Barreiro, J. López-Beceiro, J. Tarrío Saavedra, S. Naya and R. Artiaga, *Polym. Test.*, 2010, **29**, 1002.

49 S. H. Song, Y. Hao, H. S. Dong, J. M. Li and C. J. Explos, *Propellants*, 2001, **24**, 56–57.

50 W. Wang, H. Wang and J. Chen, *Macromolecules*, 2024, **57**, 2205–2217.

51 X. Zhao, Q. Zhu, J. Zou, W. Wang, R. Zeng, L. Zhao, W. Ji and Z. Fu, *J. Eur. Ceram. Soc.*, 2024, **44**, 4875–4886.